Energy-participation-ratio analysis for very anharmonic superconducting circuits

Figen Yilmaz,[1,*] Siddharth Singh,[1] Martijn F.S. Zwanenburg,[1] Jinlun Hu,[1]
Taryn V. Stefanski,[1,2] and Christian Kraglund Andersen[1]

[1] *QuTech and Kavli Institute of Nanoscience, Delft University of Technology, 2628 CJ Delft, The Netherlands*
[2] *Quantum Engineering Centre for Doctoral Training, H. H. Wills Physics Laboratory and Department of Electrical and Electronic Engineering, University of Bristol, BS8 1FD Bristol, United Kingdom*

(Received 9 January 2026; accepted 5 March 2026; published 8 April 2026)

Superconducting circuits are being used for large-scale quantum devices, and a major challenge is to perform accurate numerical simulations of device parameters. One of the most advanced methods for analyzing superconducting circuit designs is the energy-participation-ratio (EPR) method, which constructs quantum Hamiltonians based on the energy distribution extracted from classical electromagnetic simulations. In the EPR approach, we extract linear terms from finite-element simulations and add nonlinear terms using the energy participation ratio extracted from the classical simulations. However, the EPR method relies on a low-order expansion of nonlinear terms, which is prohibitive for accurately describing highly anharmonic circuits. An example of such a circuit is the fluxonium qubit, which has recently attracted increasing attention due to its high lifetimes and low error rates. In this work, we extend the EPR approach to effectively address highly nonlinear superconducting circuits, and, as a proof of concept, we apply our approach to a fluxonium qubit. Specifically, we design, fabricate, and experimentally measure a fluxonium qubit coupled to a readout resonator. We compare the measured frequencies of both the qubit and the resonator to those extracted from the EPR analysis, and we find an excellent agreement. Furthermore, we compare the dispersive shift as a function of external flux obtained from experiments with our EPR analysis and a simpler lumped-element model. Our findings reveal that the EPR results closely align with the experimental data, providing more accurate estimations compared to the simplified lumped-element simulations.

DOI: 10.1103/1rbn-c4xf

I. INTRODUCTION

Superconducting qubits are widely regarded as one of the leading platforms for implementing large-scale quantum processors [1–9]. Superconducting circuits typically consist of linear components such as capacitors and inductors as well as nonlinear elements formed by Josephson junctions. To successfully build large-scale quantum devices, we must have a precise understanding of the Hamiltonian parameters of the system. However, the nonlinear energy of the Josephson junctions prohibits the use of fully classical methods, such as finite-element simulation, to capture the relevant quantum interactions.

So far, several methods have been used and improved to extract the parameters of superconducting quantum devices using a combination of classical and quantum methods. A common approach is to describe the quantum circuits using lumped-element models, quasilumped models or continuum limits of lumped models in which the nonlinear components can be introduced in terms of discrete modes in the circuit [10–22]. The challenge of these methods is to accurately translate real physical designs into effective model parameters. An alternative approach that solves this challenge is to analyze the device design with a black-box approach using classical finite-element simulations of the device as a basis for the quantization of the device [23–25]. The energy-participation-ratio (EPR) method is an example of a method from the latter class, which uses the classical energy eigenmodes of a circuit as a basis for building the quantum Hamiltonian. The EPR method reintroduces nonlinear elements to the classical energies through a perturbative expansion, which has proven to be very effective for the widely used transmon qubit [26,27], which exhibits weak anharmonicity. However, highly anharmonic qubits, such as the fluxonium qubit [28,29], have recently gained significant traction due to their very high lifetimes and gate fidelities [30–33]. Modeling these circuits using black-box methods is an open question and requires further advancements.

*Contact author: f.yilmaz@tudelft.nl

In this work, we address the specific challenges of extracting Hamiltonian parameters for highly anharmonic superconducting quantum circuits. In particular, we present our implementation for fluxonium qubits. As a proof of concept, we design, fabricate, and measure a fluxonium qubit, and we compare the results of our extended EPR method with the experimental data. Unlike lumped-element models, which treat all superconducting islands as equipotential surfaces and cannot capture the real physical mode distribution, which may impact the effective inductive and capacitive energies of the system, our extended EPR method incorporates the full mode distribution of the circuit. Our method allows us to accurately extract Hamiltonian parameters and describe nonlinear couplings, including dispersive shifts. We demonstrate a strong correspondence between the EPR simulations and the experimentally measured resonator and qubit frequencies. Moreover, the nonlinearity of the qubit also gives rise to a nonlinear coupling between the resonator and the qubit in the form of a dispersive shift. Therefore, we also analyze the dispersive shift as predicted by the extended EPR method, and we again demonstrate great alignment with the experimentally measured dispersive shift.

This paper is structured as follows: Sec. II introduces the improved EPR method and its application to very anharmonic superconducting circuits. Section III covers the design of fluxonium qubits. Section IV presents the experimental measurements and compares them with EPR simulation results. Section V concludes with a summary of our findings and implications for future work.

II. ENERGY PARTICIPATION RATIO

In this section, we briefly explain how the EPR [25] analysis framework works and then demonstrate this method for highly anharmonic superconducting circuits [28,34,35]. The EPR method aims to provide a quantum Hamiltonian for a quantum device design through the analysis of the classical electromagnetic energy distribution. We generally design superconducting quantum devices using patterned superconducting structures, which can be combined with lumped elements. While we can treat the distinction between distributed (linear) circuits and lumped (and potentially nonlinear) circuits in broad terms for now, of note, we often encounter effective lumped elements based on Josephson junctions [36,37]; see, for example, the fluxonium qubit [28] device in Fig. 1.

For electrical circuits, the linear part of a quantum Hamiltonian is equivalent to the classical Hamiltonian. Therefore, it is often convenient to split the Hamiltonian into linear and nonlinear parts

$$H_{\text{full}} = H_{\text{lin}} + H_{\text{nl}}. \tag{1}$$

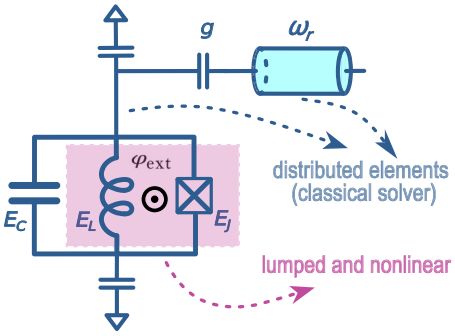

FIG. 1. The fluxonium consists of a linear inductor with the inductive energy E_L, a Josephson junction with a Josephson energy E_J, and a capacitor with a charging energy E_C. The fluxonium is capacitively coupled to a readout resonator with angular frequency ω_r. The capacitive elements as well as the readout resonator (blue) can be simulated using classical finite-element solvers, while the inductor and Josephson junction (pink) are represented by lumped elements.

The linear part of the Hamiltonian contains only quadratic terms, which we split into two parts

$$H_{\text{lin}} = H_{\text{dis}} + H_{\text{lum}}, \tag{2}$$

where H_{dis} denotes the quadratic terms representing the distributed elements of the circuit, while H_{lum} represents the linear parts of the lumped structures added to the circuit. Note that the eigenmodes of the linear circuit can be fully obtained from classical finite-element methods. For now, we assume that only inductive lumped elements are added to the circuit, and we write

$$H_{\text{lum}} = \frac{1}{2}\sum_j E_j\,(2\pi\,\Phi_j\,/\,\Phi_0)^2, \tag{3}$$

with E_j being the inductive energy of element j, and Φ_j is the flux change across that element, equal to the time integral of the voltage difference across the element. Finally, Φ_0 is the magnetic flux quantum.

With the classical and linear terms set up, we can start building the quantum Hamiltonian. First, we can readily find the normal modes of the classical Hamiltonian and, thus, write the quantum Hamiltonian as a sum of quantum harmonic oscillators. The frequencies of each harmonic oscillator mode correspond to the classically solved normal mode frequencies. In other words, we can write the linear part of the Hamiltonian as

$$H_{\text{lin}} = \sum_m \hbar\omega_m a_m^\dagger a_m, \tag{4}$$

where ω_m and a_m are the angular frequency and the annihilation operator for mode m, respectively. Essentially, this

Hamiltonian captures both the distributed elements $H_{\rm dis}$ and the lumped-element terms in Eq. (2).

Physically, the lumped inductive elements may include Josephson junctions, arrays of Josephson junctions [28,38,39], or kinetic inductors [40–43], and therefore exhibit some degree of nonlinearity. We capture this nonlinearity with the Hamiltonian

$$H_{\rm nl} \equiv \sum_{j=1}^{J} \sum_{p=3}^{\infty} E_j c_{jp} (2\pi \Phi_j / \Phi_0)^p, \tag{5}$$

where c_{jp} represents the coefficient of the pth-order term in the expansion of the nonlinearity associated with element j. The total number of nonlinear elements is denoted with J.

Now, we can in principle combine the linear Hamiltonian with the nonlinear terms and we have the full quantum Hamiltonian readily at hand. However, in the process, we need to address several challenges. The first challenge in solving the full system is that the nonlinear part $H_{\rm nl}$ can mix all modes to high orders. As a convention [25], the expansion of the nonlinear term is often truncated to a fixed order N, resulting in the nonlinear Hamiltonian

$$H_{\rm nl} = \sum_{j=1}^{J} E_j (c_{j3}\varphi_j^3 + c_{j4}\varphi_j^4 + \dots) \tag{6}$$

$$\approx \sum_{j=1}^{J} E_j \sum_{p=3}^{N} c_{jp} \varphi_j^p, \tag{7}$$

with $\varphi_j = 2\pi \Phi_j / \Phi_0$ introduced here for brevity. However, for very anharmonic systems, the truncation to a fixed number of nonlinear terms leads to significant errors in the calculated energies. As an example of a system that is noteworthy [30,32,44,45] and highly nonlinear is the system that we consider in Fig. 1, which depicts a fluxonium qubit capacitively coupled to a readout resonator with a coupling strength g. Here, the nonlinearity arises from a single nonlinear lumped element. Therefore, we simply express the nonlinear Hamiltonian specifically for a single Josephson junction

$$H_{\rm nl} = -E_j [\cos(\varphi_j) + \varphi_j^2/2], \tag{8}$$

with no further approximations at this point and where φ_j coincides with the phase difference across the junction. The next challenge appears since we need to define the quantum operator φ_j. We can use the classically solved eigenmodes as a basis to express this operator as

$$\varphi_j = \sum_{m=1}^{M} \varphi_{mj} (a_m^\dagger + a_m), \tag{9}$$

where φ_{mj} is the quantum zero-point fluctuation (ZPF) of the junction phase in mode m.

Currently, the challenge remains to find the ZPF for each mode in the junction φ_{mj}, which we cannot directly extract from a classical simulation. However, in this context, the EPR offers a practical solution. We define the EPR as

$$p_{mj} \equiv \frac{\text{Inductive energy stored in junction } j}{\text{Total inductive energy stored in mode } m} \tag{10}$$

$$= \frac{\langle \psi_m | \, \frac{1}{2} E_j \varphi_j^2 \, | \psi_m \rangle}{\langle \psi_m | \, \frac{1}{2} H_{\rm lin} \, | \psi_m \rangle}, \tag{11}$$

where ψ_m is a quantum state with one Fock excitation in mode m while the remaining modes are in the vacuum state. In the EPR method, finite-element simulations provide us with the inductive energy in the junction, while the total inductive energy is always equal to $\hbar\omega_m/2$.

Using Eq. (11), we calculate the energy participation from the quantum Hamiltonian, which should match the classically calculated participation ratio. Now, calculations are reduced such that we compute the zero-point fluctuations (φ_{mj})

$$\varphi_{mj}^2 = p_{mj} \frac{\hbar\omega_m}{2E_j}. \tag{12}$$

Applying this expression to calculate the ZPF for each mode, we can find the nonlinear quantum Hamiltonian using Eqs. (8) and (9). Thus, we reach the full Hamiltonian at Eq. (1).

In the example presented in Fig. 1, we consider the case of a fluxonium qubit and a readout resonator, so we are interested in only two modes. We can identify the two modes from their differences in energy participation in the junction. Specifically, we refer to the modes with the highest EPR in the junction as the qubit mode, while the other mode with low EPR is the resonator mode.

To highlight the significance of treating the nonlinear element without truncation, we can consider the simple Taylor expansion in Eq. (6) and expand to the fourth order. When we only consider two modes q and r, the phase operator across the junction reads

$$\varphi_j = \varphi_{qj} (a_q^\dagger + a_q) + \varphi_{rj} (a_r^\dagger + a_r). \tag{13}$$

Combining the linear Hamiltonian with the fourth-order terms, we arrive at the Hamiltonian

$$H = \hbar\omega_q a_q^\dagger a_q + \hbar\omega_r a_r^\dagger a_r - \frac{E_j}{24} [\varphi_{qj} (a_q^\dagger + a_q) + \varphi_{rj} (a_r^\dagger + a_r)]^4. \tag{14}$$

By collecting the terms, we find a dispersive shift of

$$2\chi = E_j \varphi_{qj}^2 \varphi_{rj}^2 / 12. \tag{15}$$

This approach is very effective for, e.g., transmon qubits [26] due to their relatively weak anharmonicity. However,

as discussed above, we are focusing on fluxonium qubits, which have large anharmonicity. Concretely, we therefore implement the exact cosine through the matrix exponential of the junction operators. For the circuit shown in Fig. 1, the nonlinearity comes, as mentioned before, from a single Josephson junction. Additionally, an external magnetic flux is threaded through the loop formed by the Josephson junction and the linear inductor. The classical simulations cannot capture the (nonlinear) effects of the external flux, thus we include the external flux into the nonlinear term associated with the Josephson junction. Therefore, as also implemented for lumped circuits in Ref. [46], the exact nonlinear term can be written as

$$H_{\mathrm{nl}} = -E_j[\cos(\varphi_j - \varphi_{\mathrm{ext}}) + \varphi_j^2/2] \tag{16}$$

$$= -\frac{E_j}{2}\left(\exp\{i[\varphi_{qj}(a_q^\dagger + a_q) + \varphi_{rj}(a_r^\dagger + a_r)]\}e^{-i\varphi_{\mathrm{ext}}} + \mathrm{h.c.}\right) - \frac{E_j}{2}\varphi_j^2, \tag{17}$$

where $\varphi_{\mathrm{ext}} = 2\pi\Phi_{\mathrm{ext}}/\Phi_0$ is the external phase bias arising from the external flux Φ_{ext} and φ_j is the Josephson phase operator. We define the harmonic oscillator basis for the eigenmodes such that we express a_q as a matrix in the Fock basis and then the exponential term above refers to the matrix exponential in the Fock basis of the eigenmodes. For our circuit of interest, there is no analytical expression for the dispersive shift [46]. Instead, we need to diagonalize the full Hamiltonian and calculate the dispersive shift from the eigenvalues. With the eigenenergies numerically found, we can identify the dispersive shift as

$$2\chi = (\omega_{|1,1\rangle} - \omega_{|1,0\rangle}) - (\omega_{|0,1\rangle} - \omega_{|0,0\rangle}), \tag{18}$$

where $\omega_{|q,r\rangle}$ is the angular frequency for the eigenstate $|q,r\rangle$ corresponding to q and r excitations in the qubit and the resonator, respectively. It is worth mentioning that the states $|q,r\rangle$ are eigenstates of the coupled systems and not necessarily Fock states. Numerically, we first identify the resonator occupation by finding the states with maximum overlap to the state $(a_r^\dagger)^n|0,0\rangle/\sqrt{n!}$, where $|0,0\rangle$ is the readily found ground state of the system. Once the resonator excitations are identified, we can assign the qubit excitations in ascending order.

Ultimately, through the EPR method, we extracted both the linear and nonlinear terms of the system's Hamiltonian, thereby identifying all of the device's Hamiltonian parameters.

III. FLUXONIUM QUBIT DESIGN

As discussed in the previous section, our extended approach to performing the EPR analysis is expected to be relevant for the prediction of the frequencies of a highly anharmonic system as well as the prediction of nonlinear interactions with such a system. Therefore, we aim to experimentally verify our approach using a circuit consisting of a fluxonium qubit capacitively coupled to a coplanar waveguide resonator (see Fig. 2).

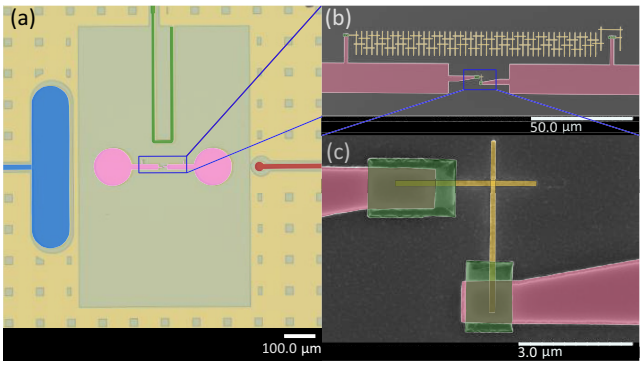

FIG. 2. (a) False-colored optical image of a fluxonium device. The pink pads represent the two superconducting islands of the fluxonium qubit, the blue pad indicates the readout pad connected to a coplanar waveguide resonator, and the green and red lines denote the flux bias and charge lines of the fluxonium qubit, respectively. The yellow area represents the ground plane of the device, while the gray area corresponds to the silicon substrate. (b) A scanning electron microscope (SEM) image with the Al junctions is shown in yellow, and Al contacts are shown in green. The central Josephson junction is located at the bottom and at the top is an array of 100 Josephson junctions, which implements a large inductance. (c) The SEM image of the central Josephson junction is shown in yellow and, as in (b), the green pads are Al contacts.

The fluxonium qubit is defined by three energy parameters: the Josephson-junction energy, $E_J = (\hbar/2e)^2/L_J$, where L_J is the inductance of the Josephson junction. The inductive energy of the inductor is $E_L = (\hbar/2e)^2/L$, where L is the inductance. Lastly, the charging energy is defined by $E_C = e^2/(2C)$, where C is the total capacitance of the qubit. We designed a floating fluxonium qubit where two circular-shaped pads provide the capacitance energy (E_C), the Josephson energy (E_J) comes from the single Josephson tunnel junction, and the inductive energy (E_L) is achieved with a hundred Josephson junctions in series (see Fig. 2). With this design, there is an inductive loop between the small Josephson junction and the Josephson-junction array. The green line represents the external flux line carrying a dc current, which generates a magnetic field that penetrates the loop of the fluxonium qubit. This magnetic field threads the loop, setting the flux to Φ_{ext}. We define the external flux as $\varphi_{\mathrm{ext}} = 2\pi\Phi_{\mathrm{ext}}/\Phi_0$, where $\Phi_0 = h/2e$ is the magnetic-flux quantum.

The fluxonium studied in this work, as shown in Fig. 2(a), is fabricated using a base metalization of NbTiN on a silicon substrate. The capacitive and coplanar waveguide structures are defined through selective etching of the NbTiN layer. To facilitate flux trapping, small squares

are added to the ground plane, acting as flux-trapping holes [47]. Both the Josephson-junction array and the small Josephson junction, shown in Figs. 2(b) and 2(c), are fabricated using a Manhattan-style layout (yellow) during the same Al deposition process [48]. Each Josephson junction in the array has an area of $(410\ \text{nm})^2$, and the small Josephson junction has an area of $(120\ \text{nm})^2$, see also Fig. 2(c). Galvanic contact between the junction electrodes and the NbTiN is ensured using Al patches, see Figs. 2(b) and 2(c) [49]. Further detailed fabrication steps are outlined in Appendix B.

We proceed by detailing the design process of the fluxonium qubit. We use the open-source `IBM QISKIT METAL` framework to construct the device layout and perform finite-element electromagnetic simulations. The designed structure is then rendered into `ANSYS HFSS`, which performs eigenmode simulations of the full design. The results of these simulations are then automatically processed using the extended EPR method presented in Sec. II. The charging energy of the fluxonium is controlled by the size of the capacitor pads and the distance to the ground plane. More generally, we find the charging energy from the full capacitance network which can similarly be extracted from the finite-element simulations using `ANSYS Q3D`. In particular, we fix the design of the fluxonium such that $E_C/(2\pi) = 0.943$ GHz based on a lumped-element model. Moreover, as we discuss further below, the capacitance matrix can also be used to extract the coupling strength g between the fluxonium and the readout resonator, see also Appendix A. A key point is that the eigenmode simulations include lumped inductive elements that represent both the Josephson junctions and the junction array. However, since the simulations are classical simulations, only the linear part of these elements are added to the simulation. The nonlinear parts are, as discussed above, added through the EPR analysis. In the numerical simulations, we have also added a lumped capacitive element to represent the capacitance of the Josephson junction. Conventionally, the junction capacitance has often been omitted in EPR analyses of superconducting circuits since most previous studies have focused on transmon circuits. Transmon qubits are characterized by their small charging energy corresponding to a large shunting capacitor, thus, the additional capacitance of the Josephson junction is a small additional contribution. In contrast, for fluxonium qubits, the typical capacitance associated with the qubit mode is 10 fF or smaller, hence, the junction capacitance plays a larger role. Specifically, we include a junction capacitance (C_J) of

$$C_J = 50 \pm 12\ \text{fF}/\mu\text{m}^2 \tag{19}$$

based on the measurements in Ref. [50]. For our case, we have a Josephson junction with an area of $(120\ \text{nm})^2$ yielding a capacitance value of 0.72 fF.

IV. EXPERIMENTAL RESULTS

To test the applicability of the EPR analysis for the fluxonium qubit design presented in the previous section, we measure the device in a cryogenic setup (see Appendix C for details). We extract the resonance frequency of the readout resonator by fitting a Lorentzian response to the data obtained from spectroscopy [see blue points in Fig. 3(a)]. By varying the bias current in the flux line of the fluxonium, we tune the fluxonium and consequently the resonator, allowing us to extract the resonator frequency as a function of the external flux. At specific flux points, avoided-crossing features appear in the resonator frequency due to interactions with the higher excited states of the fluxonium [44,46].

Next, we perform two-tone spectroscopy to characterize the fluxonium frequency, see Fig. 3(c). We carry out resonator spectroscopy with the qubit prepared in the $|0\rangle$ and $|1\rangle$ states to measure the dispersive shift. When the fluxonium qubit frequency is below 1 GHz, an active reset protocol is required because the fluxonium's thermal equilibrium approaches a fully mixed state. We employ a flux-pulse-assisted reset similar to Ref. [51], where a flux pulse temporarily shifts the fluxonium to a higher frequency, causing it to relax to the $|0\rangle$ state. After reset, we apply a π pulse to prepare the qubit in the $|1\rangle$ state. We fit double Lorentzian functions to both resonator traces to account for imperfect reset and decay during readout, extracting the change in resonator frequency between the $|0\rangle$ and $|1\rangle$ states, which corresponds to twice the dispersive shift.

To characterize the qubit frequency, we continuously apply a spectroscopy tone through the charge line of the fluxonium while simultaneously sending a readout pulse at the resonator frequency. When the spectroscopy tone is on resonance with a qubit transition, a change in the readout signal is observed, allowing us to identify the qubit frequency as the frequency with the maximal response. In contrast to the readout resonator frequency, the qubit frequency shifts smoothly from around 5 GHz down to approximately 300 MHz. This smooth behaviour supports the interpretation that the avoided crossings observed in the resonator spectroscopy originate from higher excited states of the fluxonium.

Lastly, we compare the measured frequencies with those predicted by the EPR analysis. To obtain the EPR results, we have three unknown parameters require experimental input: (i) the precise resonator frequency, (ii) the Josephson energy of the fluxonium, and (iii) the inductive energy of the junction array. Starting with the resonator, its frequency is, in principle, fully defined by the geometry. However, the device is fabricated from NbTiN, which exhibits significant kinetic inductance [52], causing a slight shift in the resonator frequency. Therefore, we offset its precise value so that the simulated frequency matches the measured frequency at zero external flux.

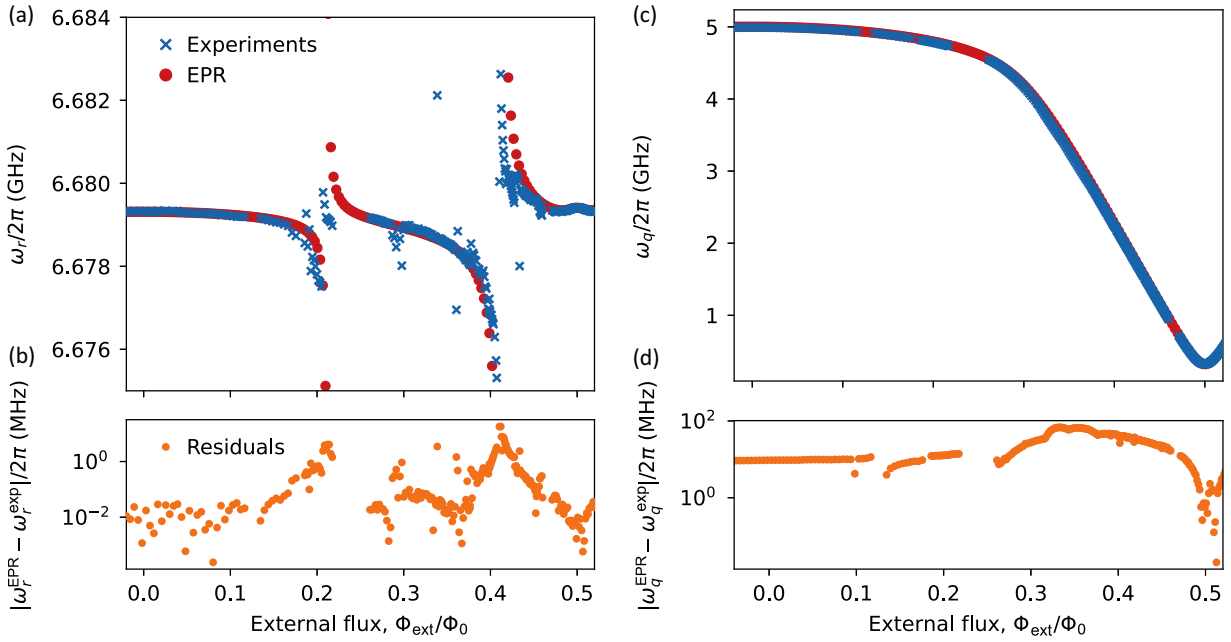

FIG. 3. (a) Resonator frequency obtained from spectroscopy measurements (blue) and the extended EPR simulations (red) as a function of the externally applied flux. (b) Qubit frequency measured by applying a spectroscopy tone to the qubit drive line while probing the resonator (blue), together with the qubit frequency extracted from the extended EPR analysis (red). (c) Residual resonator frequencies, defined as the absolute difference between EPR results and experimental data. (d) Residual qubit frequencies, defined as the absolute logarithmic difference between EPR results and experimental data.

Similarly, by analyzing the measurement data, we adjust the junction's Josephson energy and the array's inductive energy in the simulation to match the qubit frequency at zero external flux and at half a magnetic-flux quantum. We determine the values of $E_J/(2\pi) = 4.028$ GHz and $E_L/(2\pi) = 0.775$ GHz. With these energy parameters fixed, and despite initially fixing the resonator frequency at a single point, we successfully reproduce its full flux dependence, including the avoided crossings with higher excited states of the fluxonium, as shown by the red points in Fig. 3(a). In Fig. 3(b), we see the residual resonator frequencies, defined as the absolute log difference between the EPR analysis results and experimental data. The residuals remain around 10 kHz, except near the avoided crossings, where deviations naturally increase since the resonator becomes strongly nonlinear and extracting a precise resonator frequency become challenging.

Next, we perform the EPR analysis as a function of the external flux, observing excellent agreement between the simulated and measured qubit frequencies, see Fig. 3(c). In Fig. 3(d), we see that the residuals remain below 10 MHz for most of the flux range. Near $\Phi_{ext} = 0.4\Phi_0$, we observe slightly larger differences between the EPR predictions and the experimental data, which coincides with the avoided crossings with higher levels, which also renormalizes the qubit frequencies. These effects are not fully captured by the EPR simulation, likely, due to the effective coupling to higher states being inaccurate. Such inaccuracies could be because the wave function of the higher states are not accurate enough, due to the Fock-state truncation, or because the coupling is renormalized by the kinetic inductance of the qubit island.

During the EPR simulations, we truncate the Hilbert space of each eigenmode to 30 Fock states. Increasing the Hilbert space further becomes prohibitively time consuming; however, we note that the residuals in the qubit frequency at $0.5\Phi_0$ remain up to 10 MHz with 12 Fock states and reduce to below 1 MHz when increasing the truncation to 30 states. A potential limitation of the method arises if too few Fock states are used: insufficient truncation restricts an accurate description of the wave function of the higher excited fluxonium levels, leading to inaccuracies such as a poorly reproduced dispersive shift. Another possible constraint stems from fixing E_J and E_L based on the measured qubit frequencies. Since fabrication imperfections inevitably shift these parameters from their design values, requiring careful refitting to the measurement data. However, this limitation does not affect the practical applicability of our method, as we can still confirm that the targeted frequency regime is achieved across the expected range of Josephson energies.

Since the EPR approach, with the extracted Josephson and inductive energies, produces the full Hamiltonian, the model not only reproduces the qubit and resonator frequencies but also accurately captures the higher-order coupling terms. For example, the dispersive shift is a key parameter

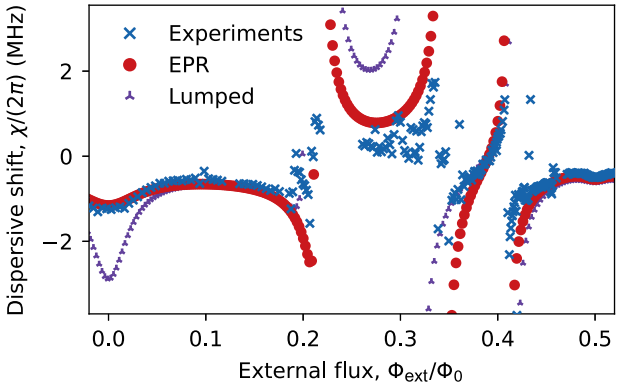

FIG. 4. Dispersive shift, denoted as χ. Here, χ is extracted as half of the difference between resonator frequency with the qubit in the excited state with the qubit in the ground state. The experimentally measured dispersive shift (blue) is compared with the EPR results (red) and the results from a lumped-element model (purple).

in the context of superconducting circuits that quantifies the mutual resonance shift between the qubit and the resonator. Due to the limited selection rules of the fluxonium, higher-order qubit levels must be considered, as they have a non-negligible impact on the dispersive shift [46]. Each higher-order level contributes to the total χ, with its contribution depending on the coupling strength g, the charge matrix element, and the detuning from the resonator.

Figure 4 compares the experimentally extracted dispersive shift (blue) with the value obtained from the EPR analysis (red). Following the method described in Sec. II, the dispersive shift is calculated directly from the EPR results. A key observation is that the EPR prediction matches the experiment remarkably well across the entire flux range, from zero external flux to half a flux quantum. Around 0.3 flux quanta, the discrepancy between the EPR results and the experimental data may originate from the fact that the experimental data is masked by the nonlinearity of the resonator near the avoided crossing with higher fluxonium levels. Alternatively, the EPR analysis may also overestimate the coupling to these higher fluxonium levels.

Up to this point, all capacitive circuit parameters, such as the charging energy E_C and the coupling strength g, have been implicitly included in the EPR simulations. Alternatively, these parameters can be obtained via electrostatic simulation followed by lumped-element modeling. To compare our extended EPR simulation with this simpler approach, we calculate E_C and g based on the lumped model, as detailed in Appendix A. Specifically, we use `ANSYS Q3D` to extract the Maxwell capacitance matrix, from which we determine the fluxonium's charging energy E_C. This matrix also provides the capacitance between the readout pad and the capacitor pads, which is essential for calculating the coupling strength g. Our calculations yield a coupling strength $g/(2\pi) = 85.15$ MHz and the charging energy $E_C/(2\pi) = 0.943$ GHz. We then configure the `scQubit` package [53,54] to model a fluxonium coupled to a resonator using the E_C and g values derived from our lumped-model calculations. Additionally, we incorporate the C_J parameter as defined in Eq. (19).

The dispersive shift extracted from the simplified lumped model follows the experimental data effectively, as indicated by the purple points in Fig. 4. However, at zero flux quantum and at flux biases around 0.2 to 0.3 flux quanta, the EPR results align much more closely with the experiments compared to the lumped model. This suggests that the lumped model is overly simplified for the circuit under study, primarily due to its assumption that all superconducting islands behave as equipotential surfaces. In contrast, the extended spatial distribution of the fluxonium mode plays a key role in renormalizing effective circuit parameters such as E_C and g. Crucially, the extended EPR analysis naturally captures this renormalization. Therefore, our extended EPR method provides a comprehensive description of the nonlinear coupling in a highly anharmonic circuit.

V. CONCLUSION

In this work, we have designed a fluxonium qubit using `QISKIT METAL` and we have extended the EPR analysis method to accurately account for the fluxonium's large anharmonicity. By comparing simulation results from the extended EPR method with experimental data, we observe excellent agreement in predicting both qubit and readout resonator frequencies. Additionally, we successfully addressed the challenge of predicting the dispersive coupling between the fluxonium qubit and the readout resonator, again demonstrating strong agreement between the simulations and the experimental data. Notably, a fully lumped-element analysis yielded less accurate predictions for the dispersive shift, highlighting the critical role of high-frequency simulations in capturing the quantum properties of superconducting devices. Looking ahead, the next apparent challenge is to integrate our method into larger circuits, for example, featuring multiple coupled fluxonium qubits and potentially tunable coupling elements. This work represents a significant step forward in the development of efficient, scalable quantum computing technologies based on highly nonlinear superconducting qubits.

ACKNOWLEDGMENTS

F.Y. designed the fluxonium device. F.Y. and S.S. fabricated the device. F.Y. and J.H. developed the EPR analysis. M.F.S.Z. and T.V.S. set up the measurement electronics and software. M.F.S.Z and S.S. measured the experimental data. M.F.S.Z. and F.Y. analyzed the data. F.Y. wrote the manuscript with input from all co-authors, and

C.K.A. supervised the work. Authors thank the following for input and preliminary work that helped enable this work: J. Parvizinejad, A. Kazmina, S. Vallés-Sanclemente, R.v.d. Boogaart, N. Papadopoulos, D. Thoen, M. Pita-Vidal, and L. Splitthoff. The authors acknowledge financial support from the Dutch Research Council (NWO). The research was partly funded through the NWO Open Competition Science project OCENW.M.23.118. T.V.S. additionally acknowledges the support of the Engineering and Physical Sciences Research Council (EPSRC) under EP/SO23607/1.

DATA AVAILABILITY

The extended EPR repository is available [55], as is the Qiskit-Metal repository [56]. All measurement data acquired during this experiment are also available [57].

APPENDIX A: CIRCUIT QUANTIZATION

In this appendix, we demonstrate how circuit quantization applies to superconducting circuits consisting of capacitors, inductors, and Josephson junctions, see Fig. 5. To establish a quantum description of an electrical circuit, we begin with the classical Lagrangian, defined as the kinetic energy minus the potential energy ($\mathcal{L} = T - U$). For electrical circuits, the capacitance energy represents the kinetic energy, while the inductive energy serves as the system's potential energy.

We define the flux (ϕ) and charge (Q) using the nodes in our quantum circuit such that

$$\phi_n(t) = \int_{-\infty}^{t} V_n(t')dt', \tag{A1}$$

where V_n denotes node voltage at node n and

$$Q_n(t) = \int_{-\infty}^{t} I_n(t')dt', \tag{A2}$$

where I_n denotes node current.

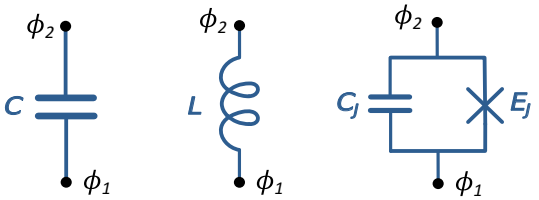

FIG. 5. The circuit elements of superconducting circuits. Two superconducting nodes ϕ_1 and ϕ_2 are connected with either a capacitor, inductor, or a Josephson junction. For the Josephson junction, we have explicitly separated the Josephson capacitance and the inductive Josephson energy for clarity.

We use the node flux as our generalized position variable and we write the Lagrangian of each element as

$$\mathcal{L}(\phi, \dot{\phi}) = \mathcal{L}_C + \mathcal{L}_L = E_{\text{cap}}(\dot{\phi}) - E_{\text{ind}}(\phi). \tag{A3}$$

In practice, we construct this Langragian by summing up the energies of all elements in the circuit. Specifically, for a capacitor connection between two nodes, ϕ_1 and ϕ_2, we have the capacitive energy

$$E_{\text{cap}}(\dot{\phi}_1, \dot{\phi}_2) = \frac{C}{2}(\dot{\phi}_1 - \dot{\phi}_2)^2. \tag{A4}$$

Similarly, for an inductor connecting nodes ϕ_1 and ϕ_2, we have

$$E_{\text{ind}}(\phi_1, \phi_2) = \frac{(\phi_1 - \phi_2)^2}{2L}. \tag{A5}$$

The next step is to introduce the Josephson junction.

The Josephson junction is characterized by a Josephson capacitance that simply takes the form of Eq. (A4) and an additional inductive energy

$$E_{JJ}(\phi_1, \phi_2) = -E_J \cos\left(2\pi \frac{\phi_1 - \phi_2}{\phi_0}\right), \tag{A6}$$

where ϕ_0 is the magnetic-flux quantum.

After writing each element's Lagrangian, we are ready to quantize a fluxonium qubit coupled to a resonator. This approach allows us to derive the coupling strength, resonator frequency, and other relevant parameters.

For the circuit diagram of our design, see Fig. 6, we start with the Lagrangian written as

$$\begin{aligned}\mathcal{L} = &\frac{C_q}{2}(\dot{\phi}_1 - \dot{\phi}_2)^2 + \frac{C_1}{2}\dot{\phi}_1^2 + \frac{C_2}{2}\dot{\phi}_2^2 + \frac{C_r}{2}\dot{\phi}_r^2 \\ &+ \frac{C_{qr}}{2}(\dot{\phi}_2 - \dot{\phi}_r)^2 + E_J \cos\left(2\pi \frac{\phi_1 - \phi_2}{\phi_0}\right) \\ &- \frac{1}{2L_q}(\phi_1 - \phi_2)^2 - \frac{1}{2L_r}\phi_r^2.\end{aligned} \tag{A7}$$

For convenience, we can write the capacitance part in matrix form such that the Lagrangian reads

$$\begin{aligned}\mathcal{L} = &\frac{1}{2}\vec{\dot{\phi}}^T \mathbb{C} \vec{\dot{\phi}} + E_J \cos\left(2\pi \frac{\phi_1 - \phi_2}{\phi_0}\right) \\ &- \frac{1}{2L_q}(\phi_1 - \phi_2)^2 - \frac{1}{2L_r}\phi_r^2,\end{aligned} \tag{A8}$$

with the matrix

$$\mathbb{C} = \begin{pmatrix} C_1 + C_q & -C_q & 0 \\ -C_q & C_2 + C_q + C_{qr} & -C_{qr} \\ 0 & -C_{qr} & C_r + C_{qr} \end{pmatrix}. \tag{A9}$$

We now make the substitution $\phi = \phi_1 - \phi_2$, $\phi_\Sigma = \phi_1 + \phi_2$, and $\phi_r = \phi_r$, which is described by the transformation

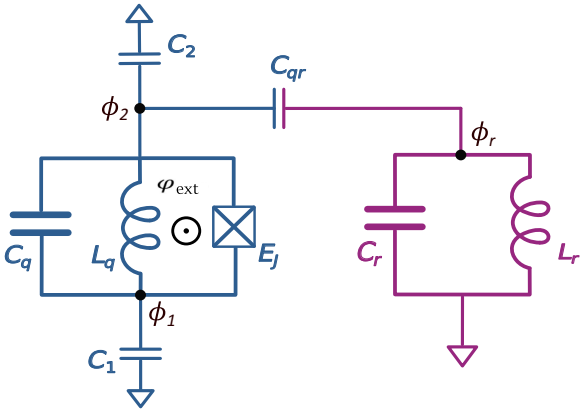

FIG. 6. A circuit diagram of the fluxonium qubit capacitively coupled to a resonator. The fluxonium is characterized by a Josephson energy E_J, an inductor with an inductance L_q, and a capacitor C_q, which includes the junction capacitance. Additionally, each fluxonium island has a capacitive connection to the ground. The resonator is here described as a lumped oscillator with capacitance C_r and inductance L_r. The resonator and the fluxonium are capacitively coupled by a capacitance C_{qr}.

matrix

$$\mathbb{M} = \begin{pmatrix} 1 & -1 & 0 \\ 1 & 1 & 0 \\ 0 & 0 & 1 \end{pmatrix}. \tag{A10}$$

Using this transformation, the Lagrangian becomes

$$\mathcal{L} = \frac{1}{2}[\dot{\phi}, \dot{\phi}_\Sigma, \dot{\phi}_r]\tilde{\mathbb{C}}[\dot{\phi}, \dot{\phi}_\Sigma, \dot{\phi}_r]^T + E_J \cos\left(2\pi \frac{\phi}{\phi_0}\right) - \frac{1}{2L_q}\phi^2 - \frac{1}{2L_r}\phi_r^2, \tag{A11}$$

where we have the transformed capacitance matrix

$$\tilde{\mathbb{C}} = \begin{pmatrix} \frac{C_1+C_2+C_{qr}}{4} + C_q & \frac{C_1-C_2-C_{qr}}{4} & C_{qr}/2 \\ \frac{C_1-C_2-C_{qr}}{4} & (C_1+C_2+C_{qr})/4 & -C_{qr}/2 \\ C_{qr}/2 & -C_{qr}/2 & C_r + C_{qr} \end{pmatrix}. \tag{A12}$$

From here, we can find the conjugate variables as

$$\vec{q} = \tilde{\mathbb{C}}[\dot{\phi}, \dot{\phi}_\Sigma, \dot{\phi}_r]^T, \tag{A13}$$

which leads to the Hamiltonian

$$H = \frac{1}{2}\vec{q}^T\tilde{\mathbb{C}}^{-1}\vec{q} - E_J \cos\left(2\pi \frac{\phi}{\phi_0}\right) + \frac{1}{2L_q}\phi^2 + \frac{1}{2L_r}\phi_r^2. \tag{A14}$$

Here, the charging energies are determine by the inverse capacitance matrix. Note that we can ignore ϕ_Σ terms because they do not contribute to the potential energy in the Lagrangian and, therefore, have no effect on the qubit frequency. Additionally, under the assumption $C_r \gg C_1, C_2, C_{qr}, C_q$ the relevant charging terms became

$$\tilde{\mathbb{C}}^{-1} = \begin{pmatrix} \frac{1}{C_\star} & - & \frac{1}{C_{cpl}} \\ - & - & - \\ \frac{1}{C_{cpl}} & - & \frac{1}{C_r+C_{qr}} \end{pmatrix}, \tag{A15}$$

with

$$\frac{1}{C_\star} = \frac{1}{C_q + \frac{C_1(C_2+C_{qr})}{C_1+C_2+C_{qr}}} \tag{A16}$$

and

$$\frac{1}{C_{cpl}} = \frac{-C_{qr}}{C_\star(C_{qr}+C_r)\frac{(C_1+C_2+C_{qr})}{C_1}}. \tag{A17}$$

Thus, we finally arrive at the Hamiltonian of the system

$$H = \frac{1}{2C_\star}q^2 - E_J \cos\left(2\pi \frac{\phi}{\phi_0}\right) + \frac{1}{2L_q}\phi^2 + \frac{1}{2(C_r+C_{qr})}q_r^2 + \frac{1}{2L_r}\phi_r^2 + \frac{1}{C_{cpl}}qq_r. \tag{A18}$$

We can introduce $E_C = e^2/(2C_\star)$ and $E_L = \phi_0^2/L_q(2\pi)^2$ together with the operators $n = q/(2e)$, $\varphi = 2\pi\phi/\phi_0$, $\phi_r = \sqrt{\hbar/2\omega(C_r+C_{qr})}(a^\dagger + a)$ and $q_r = i\sqrt{\hbar\omega(C_r+C_{qr})/2}(a^\dagger - a)$ such that we get the Hamiltonian of the form

$$H = 4E_C n^2 - E_J\cos(\varphi) + \frac{E_L}{2}\varphi^2 + \hbar\omega_r a^\dagger a + i\hbar g(a^\dagger - a)n. \tag{A19}$$

Here we have the resonator frequency given by

$$\omega_r = 1/\sqrt{L_r(C_r+C_{qr})}. \tag{A20}$$

In Eq. (A19), we derived the coupling strength g assuming the resonator to be a lumped LC oscillator, as shown in Fig. 6. In the design presented in the main text, however, the readout resonator is a $\lambda/2$ resonator with a large shunt capacitor introduced by the pad located close to the qubit. This large capacitance modifies the mode distribution and, consequently, the effective capacitive coupling [12]. We therefore modify the coupling g to account for these two aspects and arrive at the coupling strength

$$g = 2e\omega_r B\sqrt{\frac{Z_0}{\pi\hbar}}u_{\text{corr}}. \tag{A21}$$

Here, we rewrite the prefactor $1/C_{\text{cpl}}$ by introducing the dimensionless parameter $B = (C_r + C_{qr})/C_{\text{cpl}}$, which naturally emerges after quantization and u_{corr} is a correction

term that accounts for the precise mode distribution of the resonator. This factor can be evaluated as $u_{\mathrm{corr}} = \cos(\omega_r C_{\mathrm{pad}} Z_0)$ using the resonator impedance Z_0 and the capacitance C_{pad} that refers to the combined capacitance of the readout pad.

APPENDIX B: FABRICATION STEPS

The fabrication process for this device begins with a 4-inch high-resistivity silicon wafer (resistivity $> 20\,\mathrm{k\Omega\,cm}$) from Topsil, featuring a (1-0-0) orientation and with a thickness of 525 μm. Before metal deposition, the wafer is cleaned in nitric acid (HNO_3) accompanied by sonication for 6 min, followed by a quick dip in deionized (DI) water and then placed in a second DI water bath at room temperature (21 °C). After blow drying with N_2, the wafer is cleaned with 40% HF solution for 7 min. It is then rinsed twice with DI water—an initial quick dip to prevent ongoing etching from residual acid—before a final blow dry. Immediately afterwards, an HMDS layer is spun to alleviate oxide formation before sputtering [58].

We use an AJA sputtering system with a 3-inch Nb/Ti (0.7:0.3) target to deposit the metal layer via reactive DC magnetron sputtering. The wafer is coated with a 200 nm film under these conditions: 50 sccm Ar and 3.5 sccm N_2 plasma at a pressure of 2.3 mtorr and a power of 250 W. We then spin coat the dicing resist (S1805) at 1000 rpm, followed by baking at 90 °C for 5 min. In the next step, the wafer is diced into $15 \times 15\ \mathrm{mm}^2$ coupons. The $15 \times 15\ \mathrm{mm}^2$ coupons are placed in N-methyl pyrrolidone (NMP), rinsed with acetone and isopropyl alcohol (IPA), and blow dried with N_2.

To define the structures in the base metalization, an AR.P 6200.18 resist is spun at 2500 rpm and baked for 3 min. The resist is patterned using a 100 keV Raith E-beam lithography system, operating with a beam current of 256 nA and a dose of 350 $\mu\mathrm{C/cm}^2$. The pattern is developed using a sequence of solutions: pentyl acetate, followed by a 1:3 mixture of MIBK and IPA, and finally pure IPA. Each step lasts for 60 s with gentle agitation and is conducted at room temperature. Next, the NbTiN layer is selectively etched using reactive ion etching (RIE-Sentech Etchlab 2000) with a two-step etch recipe. The first step involves primarily physical etching, while the second step focuses on chemical etching to produce a smoother silicon surface. The etching recipes are as follows:

(1) 13.5 sccm SF_6 mixed with 4 sccm O_2 at 0.010 mbar pressure with 70 W of power.
(2) 4 sccm SF_6 mixed with 15 sccm O_2 at 0.080 mbar pressure with 50 W of power.

The coupon is then placed in 80 °C NMP to strip the resist overnight. Afterwards, the cleaning process is completed using acetone and IPA. Next, the coupon undergoes a 30-s BOE (1:7) dip, followed by a quick rinse in DI water and a longer soak in DI water to conclude the process. Immediately following the cleaning, a bilayer resist stack is applied to the coupon:

(1) MMA-EL8 resist, spin at 4000 rpm and bake at 185 °C for 5 min after.
(2) PMMA-950 A4 resist, spin at 2000 rpm and bake at 185 °C for 5 min after.

We use the same E-beam lithography system for the Josephson-junction structures, exposing all the junctions in a single step with a Manhattan-style pattern and an undercut profile in the bilayer stack. A beam current of 98 pA with a dose of 1200 $\mu\mathrm{C/cm}^2$ is used for junction exposure, and 129 pA with a dose of 540 $\mu\mathrm{C/cm}^2$ for the undercuts. Development is performed using a H_2O mixture at 6 °C, followed by a 40 s BOE (1:7) clean and DI water rinses lasting 10 s and 60 s, respectively.

The Josephson junctions are deposited using the Plassys MEB 550 system via a two-step aluminium evaporation process. The details of the Al deposition are as follows:

(1) The chamber is preconditioned using deposition of Ti at a rate of 0.2 nm/s until a thickness of 20 nm is reached.
(2) The first Al deposition occurs at a rate of 0.5 nm/s with a deposition angle of 55°, reaching approximately 30 nm thickness.
(3) The sample undergoes 11 min of O_2 oxidation at at 0° and 1.3 mbar.
(4) The holder is rotated by 90° for the second Al deposition, again at a rate of 0.5 nm/s and a deposition angle of 55°, until approximately 110 nm thickness is achieved.
(5) The sample undergoes another 11 min of O_2 oxidation at 0° and 1.3 mbar.

The deposition thickness is measured on the crystal, though it is expected to be thinner on the device surface

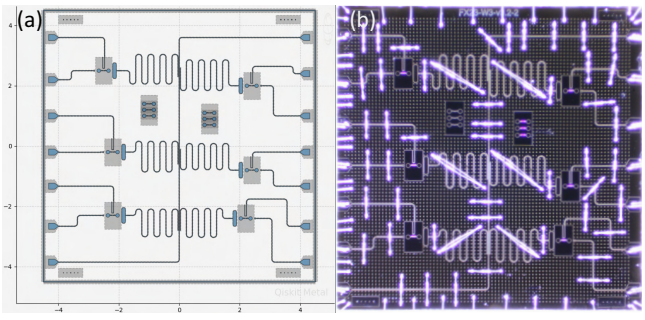

FIG. 7. A GUI image of the six single fluxonium qubit device (a) design by using `QISKIT METAL` (b) and the fabricated device with Al wire bonds.

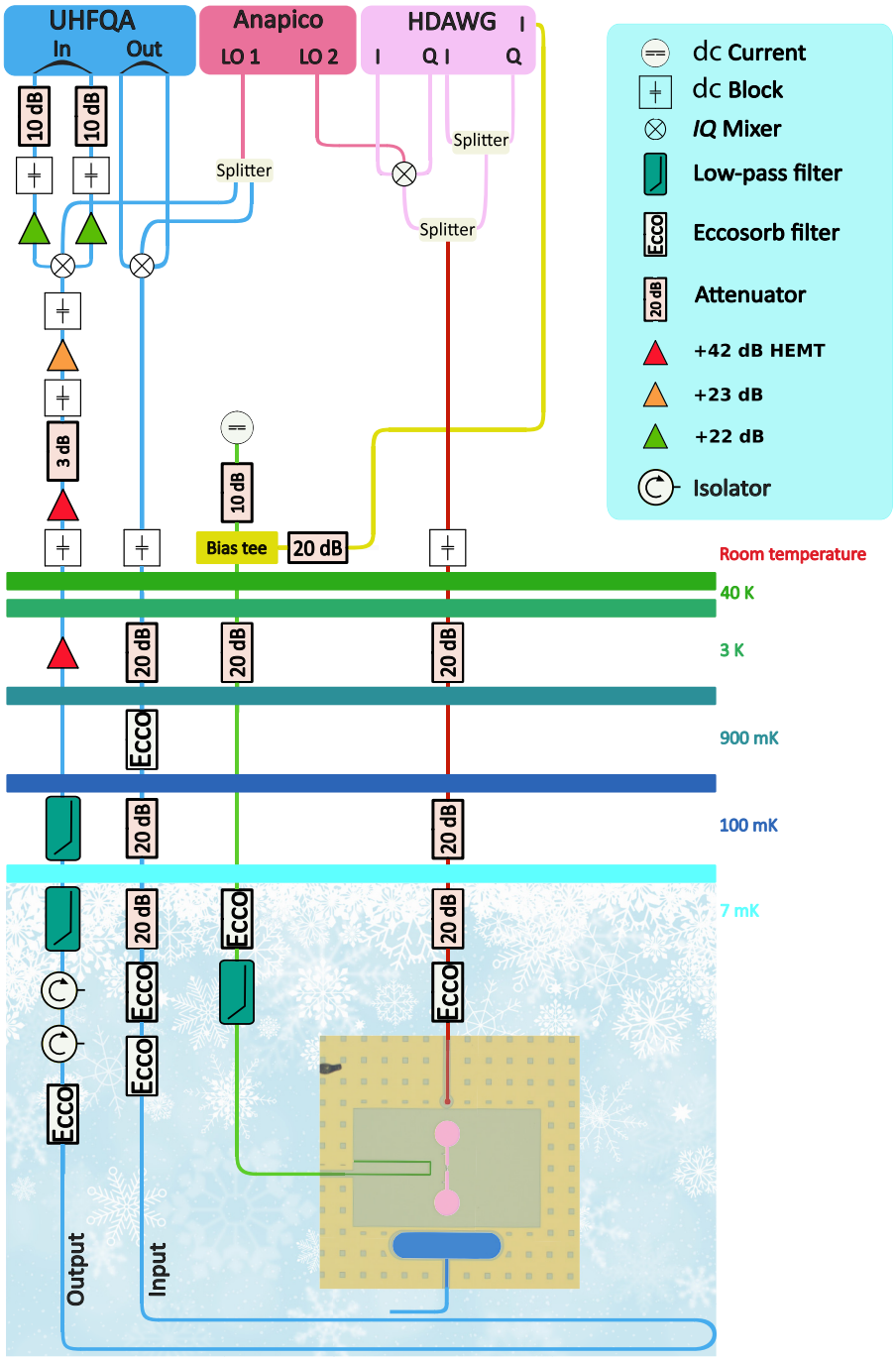

FIG. 8. Wiring diagram inside the dilution refrigerator and the room-temperature electronic setup, see details of the components in Table I, which is further discussed in the text.

due to the deposition angle. After deposition, the chip undergoes a lift-off process, during which it is soaked in acetone at 50 °C for at least 2 h. This is followed by an additional stripping step in 80 °C NMP. Finally, the chip is rinsed in succession with acetone and IPA.

After the junction fabrication is completed, patches are applied to specific areas of the junctions to improve the galvanic connection between the electrodes and the underlying metal layer (see Fig. 2). This step follows the same lithography process used for the junctions, though undercuts are not required this time. The patches are deposited using the Plassys system, beginning with a 2-min argon milling step in the load lock, followed by the deposition of 150 nm of Al at a 0° deposition angle and finishing the process with 11 min of O_2 oxidation at 0° and 1.3 mbar. The chip then undergoes a lift-off

process, utilizing the same acetone and NMP stripping method.

In the final step, we apply the dicing resist (S1805) by spinning it to achieve a PCB size of 9×9 mm^2. After dicing with the same tool, we strip the resist, and the device is released from the cleanroom, ready to be sent to the wire-bonder room.

In Fig. 7, we display the whole circuit design (a) the device from the IBM `QISKIT METAL` GUI image and (b) the fabricated device, which includes its Al wire bonds. Some of these bonds are used for grounding, while others establish the connection between the PCB and the launch pads on the device. Additionally, we incorporate six test structures in the center of the chip, enabling room-temperature probing of the junction resistance. Three of these structures host a single Josephson junction on the left, while the remaining three feature an array on the right.

APPENDIX C: MEASUREMENT SETUP

The fabricated device is diced into 9×9 mm^2 coupons, then affixed with GE varnish onto a gold-plated copper mount, and electrically connected to its printed circuit board (PCB) via 25-μm-thick Al wire bonds using a semi-automatic F&S Bondtec® equipment. Once wire bonding is completed, the device is loaded into our dilution refrigerator. For our samples, we use BLUEFORS® LD400 series, which has multiple temperature stages, as depicted in Fig. 8. The samples are mounted in the mixing chamber stage, which operates at around 7 mK. For added magnetic shielding, the device is protected on both sides by Al and the PCB is encased in two Mu-metal cans.

The device used in this paper hosts six single fluxonium qubits, six flux-bias lines, six charge lines, and six $\lambda/2$ resonators, which are capacitively coupled to the transmission line, as depicted in Fig. 7. The control electronics and measurement setup are summarised in Table I. However, only the wiring diagram for one qubit is shown, as we focus on a specific qubit for this work.

The readout signal tone is generated by a Zurich Instruments UHFQA quantum analyzer and up-converted to microwave frequencies using an *IQ* mixer, with the local oscillator (LO 1) signal supplied by the APMS20G-4 AnaPico signal generator for the up-conversion. The up-converted signal is attenuated by a series of attenuators and an Eccosorb filter before reaching the sample at base temperature. After passing through a weak Eccosorb filter, the output line includes two isolators. To filter out higher-frequency components, low-pass filters are applied at 7 and 100 mK. The signal is amplified at the 3-K stage by a 42-dB HEMT amplifier, followed by additional 42- and 23-dB amplifiers at room temperature, with a 3-dB attenuator in between to suppress standing modes. Finally, the signal is down-converted and amplified with 22-dB amplifiers on both the I and Q signals. Two 10-dB attenuators are used at the UHFQA input to match its dynamic range.

TABLE I. List of control electronics and additional equipment used at room temperature and cryogenic stages.

Dilution refrigerator	BLUEFORS® LD400
IQ mixer readout input	Zurich Instruments® HDIQ
AWG readout output/ADC	Zurich Instruments® UHFQA
AWG flux/charge line	Zurich Instruments® HDAWG
IQ mixer charge line	Marki IQ-1545LMP
IQ demodulator	QuTech-in house
rf source	APMS20G-4
dc source	QuTech-in house
Bias-tee	Mini-Circuits ZFBT-4R2GW+
dc block	Mini-Circuits BLKD-183-S+ inner-outer
Eccosorb IR filter	QuTech-in house
Isolator	LNF-ISISC4_8A s/n 2027-17 4-8 GHz
Low-pass filter	VLFX-105+
Splitter	Mini-Circuits ZX10R-14-S+ DC-10 000 MHz
−20-dB attenuator	Bluefors
−10-dB attenuator	MCL BW-S10 W2+
+22 amplifier	Mini-Circuits GALI-3+
+42 HEMT	LNF-LNC4_8C s/n 2701H

On the flux line, a 750-MHz eight-channel high-density arbitrary waveform generator (HDAWG) generates the flux pulses, while an in-house QuTech S4g current source module supplies the dc bias current. These signals were combined with a bias-tee at room temperature. Additionally, a 20-dB attenuator is included at 3 K, along with an Eccosorb and low-pass filters at the mixing chamber.

We use two slightly different hardware configurations to address the qubit above and below $\omega_q/2\pi = 1$ GHz. For frequencies above 1 GHz (as shown in Fig. 8), the HDAWG generates the *IQ* signals at an intermediate frequency for up-conversion. For qubit frequencies below 1 GHz, the drive signal is generated directly by the HDAWG. These signals are combined with a power splitter. The charge-line signal is attenuated similarly to the input line, as shown in Fig. 8.

[1] F. Arute, K. Arya, R. Babbush, D. Bacon, J. C. Bardin, R. Barends, R. Biswas, S. Boixo, F. G. Brandao, D. A. Buell *et al.*, Quantum supremacy using a programmable superconducting processor, Nature **574**, 505 (2019).

[2] Y. Wu, W.-S. Bao, S. Cao, F. Chen, M.-C. Chen, X. Chen, T.-H. Chung, H. Deng, Y. Du, D. Fan *et al.*, Strong quantum computational advantage using a superconducting quantum processor, Phys. Rev. Lett. **127**, 180501 (2021).

[3] S. Krinner, N. Lacroix, A. Remm, A. Di Paolo, E. Genois, C. Leroux, C. Hellings, S. Lazar, F. Swiadek, J. Herrmann

et al., Realizing repeated quantum error correction in a distance-three surface code, Nature **605**, 669 (2022).
[4] Y. Zhao, Y. Ye, H.-L. Huang, Y. Zhang, D. Wu, H. Guan, Q. Zhu, Z. Wei, T. He, S. Cao *et al.*, Realization of an error-correcting surface code with superconducting qubits, Phys. Rev. Lett. **129**, 030501 (2022).
[5] Q. Zhu, S. Cao, F. Chen, M.-C. Chen, X. Chen, T.-H. Chung, H. Deng, Y. Du, D. Fan, M. Gong *et al.*, Quantum computational advantage via 60-qubit 24-cycle random circuit sampling, Sci. Bull. **67**, 240 (2022).
[6] Y. Kim, A. Eddins, S. Anand, K. X. Wei, E. van sen Berg, S. Rosenblatt, H. Nayfeh, Y. Wu, M. Zaletel, K. Temme *et al.*, Evidence for the utility of quantum computing before fault tolerance, Nature **618**, 500 (2023).
[7] A. Asfaw, A. Megrant, C. Jones, C. Gidney, D. Bacon, D. Debroy, D. Kafri, E. Lucero, H. Neven, J. Hilton *et al.*, Suppressing quantum errors by scaling a surface code logical qubit, Nature **614**, 676 (2023).
[8] R. Acharya, L. Aghababaie-Beni, I. Aleiner, T. I. Andersen, M. Ansmann, F. Arute, K. Arya, A. Asfaw, N. Astrakhantsev, J. Atalaya *et al.*, Quantum error correction below the surface code threshold, Nature **638**, 920 (2025).
[9] H. Ali, J. Marques, O. Crawford, J. Majaniemi, M. Serra-Peralta, D. Byfield, B. Varbanov, B. M. Terhal, L. DiCarlo, and E. T. Campbell, Reducing the error rate of a superconducting logical qubit using analog readout information, Phys. Rev. Appl. **22**, 044031 (2024).
[10] M. H. Devoret *et al.*, Quantum fluctuations in electrical circuits, Les Houches, Session LXIII **7**, 133 (1995).
[11] A. Blais, R.-S. Huang, A. Wallraff, S. M. Girvin, and R. J. Schoelkopf, Cavity quantum electrodynamics for superconducting electrical circuits: An architecture for quantum computation, Phys. Rev. A **69**, 062320 (2004).
[12] J. Bourassa, F. Beaudoin, J. M. Gambetta, and A. Blais, Josephson-junction-embedded transmission-line resonators: From Kerr medium to in-line transmon, Phys. Rev. A **86**, 013814 (2012).
[13] M. Leib, F. Deppe, A. Marx, R. Gross, and M. J. Hartmann, Networks of nonlinear superconducting transmission line resonators, New J. Phys. **14**, 075024 (2012).
[14] H. L. Mortensen, K. Mølmer, and C. K. Andersen, Normal modes of a superconducting transmission-line resonator with embedded lumped element circuit components, Phys. Rev. A **94**, 053817 (2016).
[15] W. C. Smith, A. Kou, U. Vool, I. M. Pop, L. Frunzio, R. J. Schoelkopf, and M. H. Devoret, Quantization of inductively shunted superconducting circuits, Phys. Rev. B **94**, 144507 (2016).
[16] A. Parra-Rodriguez, E. Rico, E. Solano, and I. L. Egusquiza, Quantum networks in divergence-free circuit QED, Quantum Sci. Technol. **3**, 024012 (2018).
[17] Z. K. Minev, T. G. McConkey, M. Takita, A. D. Corcoles, and J. M. Gambetta, Circuit quantum electrodynamics (CQED) with modular quasi-lumped models, arXiv:2103.10344.
[18] A. Di Paolo, T. E. Baker, A. Foley, D. Sénéchal, and A. Blais, Efficient modeling of superconducting quantum circuits with tensor networks, npj Quantum Inf. **7**, 11 (2021).
[19] I. L. Egusquiza and A. Parra-Rodriguez, Algebraic canonical quantization of lumped superconducting networks, Phys. Rev. B **106**, 024510 (2022).
[20] A. Parra-Rodriguez and I. L. Egusquiza, Geometrical description and Faddeev-Jackiw quantization of electrical networks, Quantum **8**, 1466 (2024).
[21] A. Osborne, T. Larson, S. G. Jones, R. W. Simmonds, A. Gyenis, and A. Lucas, Symplectic geometry and circuit quantization, PRX Quantum **5**, 020309 (2024).
[22] A. Parra-Rodriguez and I. Egusquiza, Faddeev-Jackiw quantisation of nonreciprocal quasi-lumped electrical networks, arXiv:2401.09120.
[23] S. E. Nigg, H. Paik, B. Vlastakis, G. Kirchmair, S. Shankar, L. Frunzio, M. H. Devoret, R. J. Schoelkopf, and S. M. Girvin, Black-box superconducting circuit quantization, Phys. Rev. Lett. **108**, 240502 (2012).
[24] F. Solgun, D. W. Abraham, and D. P. DiVincenzo, Blackbox quantization of superconducting circuits using exact impedance synthesis, Phys. Rev. B **90**, 134504 (2014).
[25] Z. K. Minev, Z. Leghtas, S. O. Mundhada, L. Christakis, I. M. Pop, and M. H. Devoret, Energy-participation quantization of Josephson circuits, npj Quantum Inf. **7**, 131 (2021).
[26] J. Koch, T. M. Yu, J. Gambetta, A. A. Houck, D. I. Schuster, J. Majer, A. Blais, M. H. Devoret, S. M. Girvin, and R. J. Schoelkopf, Charge-insensitive qubit design derived from the Cooper pair box, Phys. Rev. A **76**, 042319 (2007).
[27] K.-H. Yu, X.-Y. Jiao, and L.-J. Jin, Using the inductive-energy participation ratio to characterize a superconducting quantum chip, Phys. Rev. Appl. **21**, 034027 (2024).
[28] V. E. Manucharyan, J. Koch, L. I. Glazman, and M. H. Devoret, Fluxonium: Single Cooper-pair circuit free of charge offsets, Science **326**, 113 (2009).
[29] L. B. Nguyen, Y.-H. Lin, A. Somoroff, R. Mencia, N. Grabon, and V. E. Manucharyan, High-coherence fluxonium qubit, Phys. Rev. X **9**, 041041 (2019).
[30] L. Ding, M. Hays, Y. Sung, B. Kannan, J. An, A. Di Paolo, A. H. Karamlou, T. M. Hazard, K. Azar, D. K. Kim *et al.*, High-fidelity, frequency-flexible two-qubit fluxonium gates with a transmon coupler, Phys. Rev. X **13**, 031035 (2023).
[31] A. Somoroff, Q. Ficheux, R. A. Mencia, H. Xiong, R. Kuzmin, and V. E. Manucharyan, Millisecond coherence in a superconducting qubit, Phys. Rev. Lett. **130**, 267001 (2023).
[32] H. Zhang, C. Ding, D. Weiss, Z. Huang, Y. Ma, C. Guinn, S. Sussman, S. P. Chitta, D. Chen, A. A. Houck *et al.*, Tunable inductive coupler for high-fidelity gates between fluxonium qubits, PRX Quantum **5**, 020326 (2024).
[33] F. Wang, K. Lu, H. Zhan, L. Ma, F. Wu, H. Sun, H. Deng, Y. Bai, F. Bao, X. Chang *et al.*, Achieving millisecond coherence fluxonium through overlap Josephson junctions, arXiv:2405.05481.
[34] Y.-H. Lin, L. B. Nguyen, N. Grabon, J. San Miguel, N. Pankratova, and V. E. Manucharyan, Demonstration of protection of a superconducting qubit from energy decay, Phys. Rev. Lett. **120**, 150503 (2018).
[35] N. Earnest, S. Chakram, Y. Lu, N. Irons, R. K. Naik, N. Leung, L. Ocola, D. A. Czaplewski, B. Baker, J. Lawrence *et al.*, Realization of a λ system with metastable states of

a capacitively shunted fluxonium, Phys. Rev. Lett. **120**, 150504 (2018).
[36] B. D. Josephson, Possible new effects in superconductive tunnelling, Phys. Lett. **1**, 251 (1962).
[37] B. D. Josephson, Supercurrents through barriers, Advan. Phys. **14**, 419 (1965).
[38] N. A. Masluk, I. M. Pop, A. Kamal, Z. K. Minev, and M. H. Devoret, Microwave characterization of Josephson junction arrays: Implementing a low loss superinductance, Phys. Rev. Lett. **109**, 137002 (2012).
[39] J. Puertas Martínez, S. Léger, N. Gheeraert, R. Dassonneville, L. Planat, F. Foroughi, Y. Krupko, O. Buisson, C. Naud, W. Hasch-Guichard *et al.*, A tunable Josephson platform to explore many-body quantum optics in circuit-QED, npj Quantum Inf. **5**, 19 (2019).
[40] T. M. Hazard, A. Gyenis, A. Di Paolo, A. T. Asfaw, S. A. Lyon, A. Blais, and A. A. Houck, Nanowire superinductance fluxonium qubit, Phys. Rev. Lett. **122**, 010504 (2019).
[41] D. Niepce, J. Burnett, and J. Bylander, High kinetic inductance NbN nanowire superinductors, Phys. Rev. Appl. **11**, 044014 (2019).
[42] L. Grünhaupt, M. Spiecker, D. Gusenkova, N. Maleeva, S. T. Skacel, I. Takmakov, F. Valenti, P. Winkel, H. Rotzinger, W. Wernsdorfer *et al.*, Granular aluminium as a superconducting material for high-impedance quantum circuits, Nat. Mater. **18**, 816 (2019).
[43] D. Rieger, S. Günzler, M. Spiecker, P. Paluch, P. Winkel, L. Hahn, J. Hohmann, A. Bacher, W. Wernsdorfer, and I. Pop, Granular aluminium nanojunction fluxonium qubit, Nat. Mater. **22**, 194 (2023).
[44] T. V. Stefanski and C. K. Andersen, Flux-pulse-assisted readout of a fluxonium qubit, Phys. Rev. Appl. **22**, 014079 (2024).
[45] W.-J. Lin, H. Cho, Y. Chen, M. G. Vavilov, C. Wang, and V. E. Manucharyan, 24 days-stable CNOT-gate on fluxonium qubits with over 99.9% fidelity, PRX Quantum **6**, 010349 (2025).
[46] G. Zhu, D. G. Ferguson, V. E. Manucharyan, and J. Koch, Circuit QED with fluxonium qubits: Theory of the dispersive regime, Phys. Rev. B **87**, 024510 (2013).
[47] B. Chiaro, A. Megrant, A. Dunsworth, Z. Chen, R. Barends, B. Campbell, Y. Chen, A. Fowler, I. C. Hoi, E. Jeffrey *et al.*, Dielectric surface loss in superconducting resonators with flux-trapping holes, Supercond. Sci. Technol. **29**, 104006 (2016).
[48] A. Potts, P. R. Routley, G. J. Parker, J. J. Baumberg, and P. A. J. de Groot, Novel fabrication methods for submicrometer Josephson junction qubits, J. Mater. Sci.: Mater. Electron. **12**, 289 (2001).
[49] A. Dunsworth, A. Megrant, C. Quintana, Z. Chen, R. Barends, B. Burkett, B. Foxen, Y. Chen, B. Chiaro, A. Fowler *et al.*, Characterization and reduction of capacitive loss induced by sub-micron Josephson junction fabrication in superconducting qubits, Appl. Phys. Lett. **111**, 022601 (2017).
[50] F. Deppe, S. Saito, H. Tanaka, and H. Takayanagi, Determination of the capacitance of nm scale Josephson junctions, J. Appl. Phys. **95**, 2607 (2004).
[51] I. N. Moskalenko, I. A. Simakov, N. N. Abramov, A. A. Grigorev, D. O. Moskalev, A. A. Pishchimova, N. S. Smirnov, E. V. Zikiy, I. A. Rodionov, and I. S. Besedin, High fidelity two-qubit gates on fluxoniums using a tunable coupler, npj Quantum Inf. **8**, 130 (2022).
[52] J. G. Kroll, F. Borsoi, K. Van Der Enden, W. Uilhoorn, D. De Jong, M. Quintero-Pérez, D. Van Woerkom, A. Bruno, S. Plissard, D. Car *et al.*, Magnetic-field-resilient superconducting coplanar-waveguide resonators for hybrid circuit quantum electrodynamics experiments, Phys. Rev. Appl. **11**, 064053 (2019).
[53] S. P. Chitta, T. Zhao, Z. Huang, I. Mondragon-Shem, and J. Koch, Computer-aided quantization and numerical analysis of superconducting circuits, New J. Phys. **24**, 103020 (2022).
[54] P. Groszkowski and J. Koch, Scqubits: A Python package for superconducting qubits, Quantum **5**, 583 (2021).
[55] The extended EPR Repository: https://github.com/AndersenQubitLab/andersen-lab-pyEPR.git.
[56] Qiskit-Metal Repository: https://github.com/AndersenQubitLab/andersen-lab-qiskit-metal.
[57] Measurement Data Repository: https://doi.org/10.4121/833e20fb-9863-4d0d-828a-d2ec44108e12.
[58] A. Bruno, G. de Lange, S. Asaad, K. L. van der Enden, N. K. Langford, and L. DiCarlo, Reducing intrinsic loss in superconducting resonators by surface treatment and deep etching of silicon substrates, Appl. Phys. Lett. **106**, 182601 (2015).